Journal of Materials Chemistry A

ROYAL SOCIETY OF CHEMISTRY

PAPER

View Article Online
View Journal | View Issue

Cite this: J. Mater. Chem. A, 2025, 13, 7357

A thermomechanically stable nanofiber separator with multiscale MOF networks towards high-efficiency ion transport†

Feifei Lan,‡[a] Huijuan Zhao, ‡*[a] Yu Jiang,[a] Cancan Jin,[a] Guodong Zhao*[a] and Lin Li*[ab]

Pursuing high-energy-density and high-safety lithium-metal batteries (LMBs) is crucial for developing next-generation high-energy storage systems. However, uncontrollable lithium (Li) dendrite growth and the unstable solid electrolyte interface (SEI) make this task rather challenging. Here, a thermomechanically stable nanofiber separator composed of 3D multiscale metal–organic framework (MOF) networks was developed by an electrospinning-assisted *in situ* self-assembly strategy. This design ingenuity lied in building close-packed ZIF-8 nanounits onto polyimide (PI) nanofiber to construct 1D well-ordered MOF nanofibers and generate monolithic 3D networks, thereby providing continuous and fast Li^+ linear transport pathways at the micrometer scale. Lewis acid sites and sub-nano pores within ZIF-8 served as ion sieves, selectively restricting larger anion movement to accelerate Li^+ transport. Density functional theory calculations further verified the higher adsorption energy for Li-solvated clusters and the de-solvation effect on the ZIF-8 surface, facilitating high-efficiency and well-distributed Li^+ intercalation. Moreover, these PI@ZIF-8 nanofiber separators contributed to constructing LiF-concentrated SEI films and reducing active Li and electrolyte consumption. Coupled with their excellent thermal stability, high mechanical strength and flexibility, potential safety accidents were effectively avoided. The resultant LMBs presented improved discharge capacity, cycling durability and stability, even under high-rate or high-temperature conditions, charting a promising course for developing high-quality nanofiber separators for advanced LMBs.

Received 1st November 2024
Accepted 27th January 2025

DOI: 10.1039/d4ta07790c

rsc.li/materials-a

1. Introduction

Over the last few decades, lithium-ion batteries (LIBs) have received widespread attention due to their versatile applications in power grid intelligence, vehicle electrification and device portability.[1–3] Nevertheless, the insufficient specific capacity of conventional LIB systems fails to satisfy the increasing demands for energy density.[4,5] Recognizing this, lithium-metal batteries (LMBs), utilizing metallic lithium (Li) anodes with ultra-high theoretical specific capacity (3860 mA h g^{-1}) and ultra-low reduction potential (−3.04 V *vs.* the standard hydrogen electrode), show immense potential as advanced energy storage devices.[6,7] Despite such great superiorities, the uncontrollable growth of dendritic Li and strong side reactions between active Li and liquid electrolyte are adverse to the smooth progress of Li deposition/stripping behaviors, resulting in low coulombic efficiency (CE), severe capacity degradation and even potential safety issues, consequently restricting the large-scale industrial development of LMBs.[8,9]

As one of the critical components of LMBs, separators can not only provide physical separation between the cathodes and anodes to protect against the internal short-circuits, but also allow rapid Li^+ transmission through electrolytes, which play an indispensable role in electrochemical performances and safety practicality of batteries.[10,11] Currently, commercial polyolefin separators, such as polyethylene (PE) and polypropylene (PP), still pose a risk of thermal runaway under high-temperature conditions because of their inferior thermal stability and flammability.[12] Moreover, the widely distributed pore sizes and limited electrolyte wettability of polyolefin separators will provoke uneven Li^+ distribution during continuous charging/discharging processes, easily causing the excessive growth of Li dendrites and the hazard of separators being punctured, thus culminating in inoperable redemptive consequences.[13–15] Therefore, substantial efforts have been devoted to designing high-quality separators with well-defined microstructures to meet the ever-increasing safety demands of batteries.[16]

[a]College of Textiles and Clothing, State Key Laboratory of Bio-Fibers and Eco-Textiles, Qingdao University, Qingdao 266071, P. R. China. E-mail: hjzhao@qdu.edu.cn; zhaoguodong@qdu.edu.cn

[b]Beijing Key Laboratory of Energy Conversion and Storage Materials, College of Chemistry, Beijing Normal University, Beijing 100875, P. R. China. E-mail: lilinll@bnu.edu.cn

† Electronic supplementary information (ESI) available. See DOI: https://doi.org/10.1039/d4ta07790c

‡ Both authors contributed equally to the manuscript.

Polyimide (PI), as a typical high-performance engineering polymer, possesses good chemical stability, high mechanical strength, a low dielectric coefficient, excellent temperature resistance, and insulation and self-extinguishing characteristics, making it an ideal candidate for the separator substrates of batteries.[17,18] For example, PE separators had been coated with PI substances to improve their mechanical strength, thermodimensional stability and electrolyte-uptake capability.[19,20] Besides, some novel thermostable separators based on PI substrates had also been prepared *via* phase inversion or colloidal template methods to afford superior electrochemical performances of LMBs.[21,22] In recent years, electrospun nanofiber materials have been employed in a wide application of fields, such as optical sensors, drug carriers, eco-waste purifiers and energy storage systems.[23] More importantly, electrospinning can well combine multiple polymers or functional fillers together, making it easy to construct hybridized nanofiber separators with controllable structures and characteristics.[24,25] Based on electrospinning technology, the resultant PI nanofiber separators possess three-dimensional (3D) interconnected nano-porous network structures, with high porosity, large specific area and excellent electrolyte affinity, showing a promising prospect in homogenizing Li deposition/stripping behaviors.[26,27] However, they still suffer from insufficient ionic conductivities and fail to meet the increasingly stringent requirements for high-rate LMBs. Metal–organic frameworks (MOFs) are composed of inorganic metal ions and organic ligands, equipped with high specific surface area, adjustable and uniform cavity sizes/pore windows, plentiful coordinate metal sites and periodical crystalline structures, which have been developed as prospective modified fillers for separators.[28–30] The homogeneous pores with ordered arrangement of MOFs provide well-defined Li^+ transport pathways, while their narrow channels and rich Lewis acid sites can selectively confine the movement of larger Li-salt anions, thereby promoting uniform Li^+ flux and accelerating Li^+ migration.[31–33]

In spite of the above privileges of MOFs, the enhancement in ionic conductivity is still restricted when MOF fillers are simply and physically attached to separators, as these incorporated MOFs tend to result in unfavorable aggregation and precipitation phenomena in the wake of solvent evaporation, triggering isolated and discontinuous Li^+ channels.[34,35] Additionally, the randomly distributed MOFs within separators cannot provide effective mechanical reinforcement for Li dendrite suppression.[36] Therefore, it remains challenging to realize dendrite-free Li deposition and beneficial SEI chemistry through separator modification, and the control for spatial arrangement of MOFs in separators to build a uniformly distributed MOF network is still urgent. The fabrication of intertwined nanofiber membranes anchored with active fillers assisted by the electrospinning method is deemed a promising strategy for achieving a 3D filler framework within separators, which is mainly attributed to the directional arrangement of MOF fillers that can be anticipated under the guidance of 1D nanofibers.[37] Nonetheless, the exploitation of practically available strategies for constructing nanofiber separators, based on 3D MOF networks with long-range ordered structures and favorable mechanical flexibility, still requires tremendous efforts, enabling successive and high-efficiency Li^+ transmission as well as enhanced dendrite suppression capability.[38]

Herein, a thermomechanically stable PI-supported nanofiber separator with densely packed MOF nanounits was constructed through an electrospinning-assisted *in situ* self-assembly strategy. The 3D cross-linked networks composed of 1D PI nanofiber substructures offered spatial guidance for directional self-assembly of MOFs and induced the continuous growth of MOF nanounits, thereby achieving the effective construction of 3D multiscale MOF networks. A zeolite imidazole framework (ZIF-8) was chosen as a targeted MOF due to its simple synthesis, low cost and outstanding electrochemical stability and featured large-sized cavities and orderly arranged member rings (MRs) to realize homogenized and accelerated Li^+ diffusion pathways, simultaneously forming a robust SEI film without excessive consumption of electrolyte and active Li. Besides, the 3D multiscale MOF networks relied on their abundant Lewis acid sites and microporous structure that could further optimize Li^+ transport. Moreover, the de-solvation function of ZIF-8 was well testified through density functional theory (DFT) calculations, which demonstrated an increase in the Li^+ concentration across 1D channels of the 4-MR within ZIF-8, leading to rapid and well-distributed Li^+ intercalation. With these merits, the resulting PI@ZIF-8 nanofiber separators delivered fast Li^+ transport kinetics and outstanding dendritic suppression ability, coupled with excellent thermal stability and high mechanical robustness, enabling superior operating security and desired cycling durability for the assembled LMBs, thereby revealing an enticing application prospect.

2. Results and discussion

Fig. 1a shows the detailed fabrication procedures for the PI@ZIF-8 nanofiber separators. The 3D porous PI substrate composed of cross-linked 1D nanofibers was carefully chosen as the original robust support,[18,39] which was prepared by following the electrospinning process and thermal imidization treatment. Then, ZIF-8 nanounits were *in situ* self-assembled on PI nanofibers to construct the nanofiber separators with 3D multiscale MOF networks. In this regard, an alkaline-etching method was carried out to actualize the directionally grown MOFs. As shown in Fig. 1b, the imide rings of PI underwent a cleavage reaction to generate a large number of carboxyl groups (–COOH) under the etching effect of KOH solution,[40] which provided massive and well-distributed nucleation sites to promote the formation of MOF networks with orderliness and continuum. After immersing in the methanol solution containing $Zn(NO_3)_2$, K^+ would be substituted by Zn^{2+}, which could coordinate with 2-methylimidazole to *in situ* generate ZIF-8 nanounits. Ultimately, the cleaved imide rings within the PI skeleton were re-cyclized assisted by thermal treatment, while removing the residual solvents and activating the constructed MOF networks. The as-obtained PI@ZIF-8 nanofiber separators were equipped with distinctive 3D multiscale structures, consisting of interwoven 1D MOF nanofibers. Of note, the single 1D

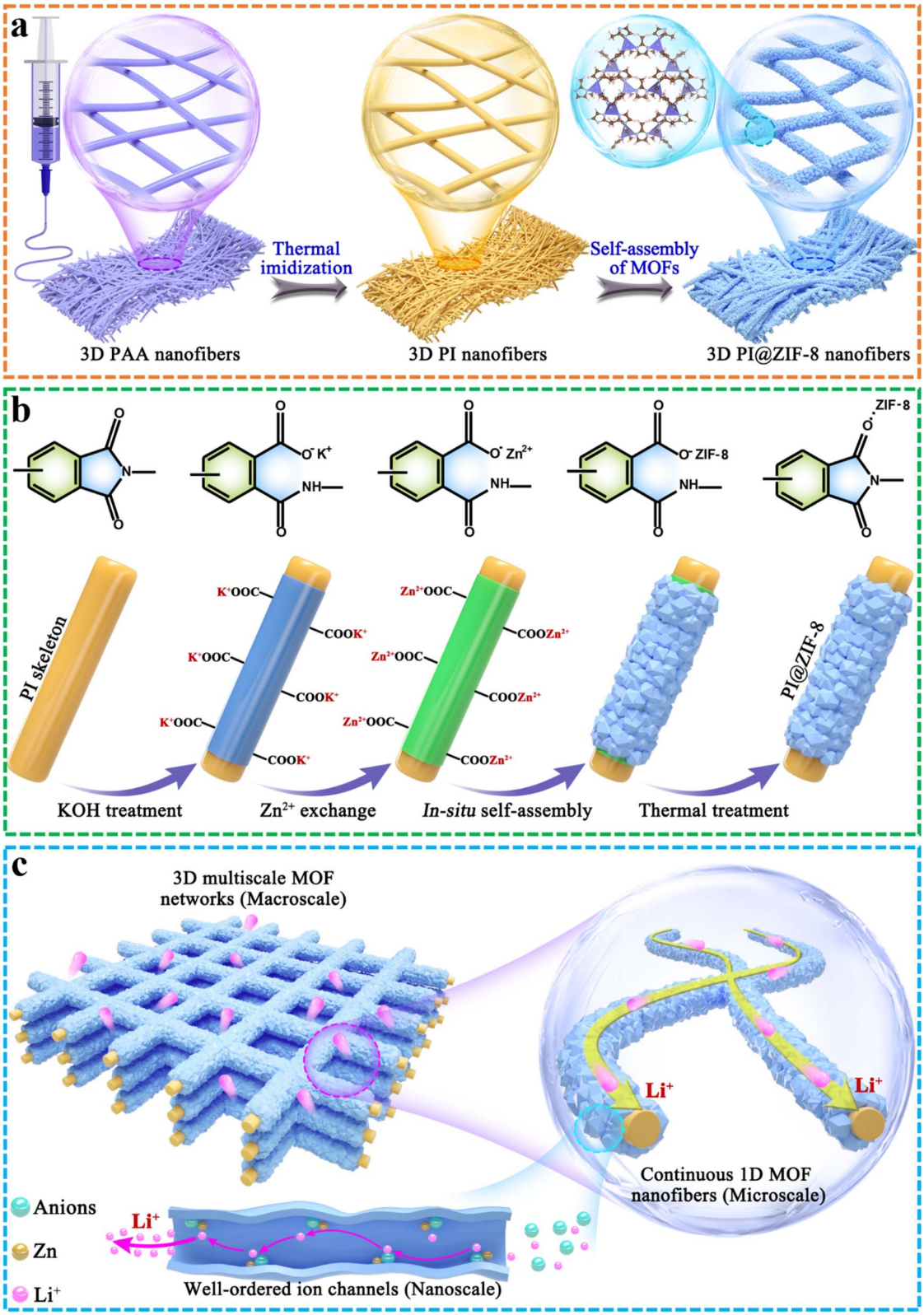

Fig. 1 Synthesis route and design concept of PI@ZIF-8 nanofiber separators with 3D multiscale MOF networks. (a) Schematic diagram for the detailed fabrication procedures of PI@ZIF-8 nanofiber separators. (b) Schematic diagram of the *in situ* self-assembly process for ZIF-8 nanounits on the PI skeleton. (c) Schematic illustration for the 3D multiscale MOF networks enabling continuous and high-efficiency Li^+ transport.

MOF nanofiber constituted ZIF-8 nanounits arranged in an orderly manner along the 1D direction at the microscale level, which could yield long-range and continuous linear channels for barrier-free and high-efficiency Li^+ transport (Fig. 1c). What was more, the nanoscale pores within MOF nanounits served as ion sieves to restrict the transmission of larger anions and conversely facilitate Li^+ migration. Meanwhile, the open metal sites on the ZIF-8 surface featuring Lewis acid characteristic could selectively bind with anions, further accelerating the free transport of Li^+.

Scanning electron microscopy (SEM) was performed to investigate the surface morphologies of the prepared polyamic acid (PAA), PI and PI@ZIF-8 nanofiber separators. Both the PAA and PI samples possessed cross-linked 3D network structures consisting of interconnected 1D nanofibers with a smooth surface (Fig. 2a and b). Further self-assembly of MOF nanounits led to the formation of continuous and symbiotic MOF shell-layers, in which the orderly arrayed ZIF-8 completely covered the PI skeleton to generate 1D MOF nanofibers (Fig. 2c and d), which played a critical role in successive ion pathways within the bulk of separators. As displayed in Fig. 2e, the energy dispersive spectroscopy (EDS) mappings demonstrated that C, N, Zn and O elements were uniformly distributed in PI@ZIF-8 nanofibers, confirming the successful self-assembly of ZIF-8 on the PI substrate to construct a typical core–shell structure. A series of characterization tests were conducted to analyze the chemical structures of the multiscale MOF networks. It could be found in Fourier transform infrared (FTIR) spectra (Fig. S1†) that PAA successfully experienced thermal imidization and was converted into PI, owing to the appearance of the typical characteristic peaks for PI. To be specific, the characteristic peaks located at 1756 and 1718 cm^{-1} corresponded to the stretching vibration of the –C═O bond on imine rings, concurrently including the stretching vibration of the C–N bond at 1376 cm^{-1} and variable angle vibration of the C═O bond and deformation vibration of imine rings at 721 cm^{-1}.[41] Moreover, the characteristic bands at 658–1300 cm^{-1} for ZIF-8 obviously appeared in the PI@ZIF-8 samples (Fig. 2f).[28] According to X-ray

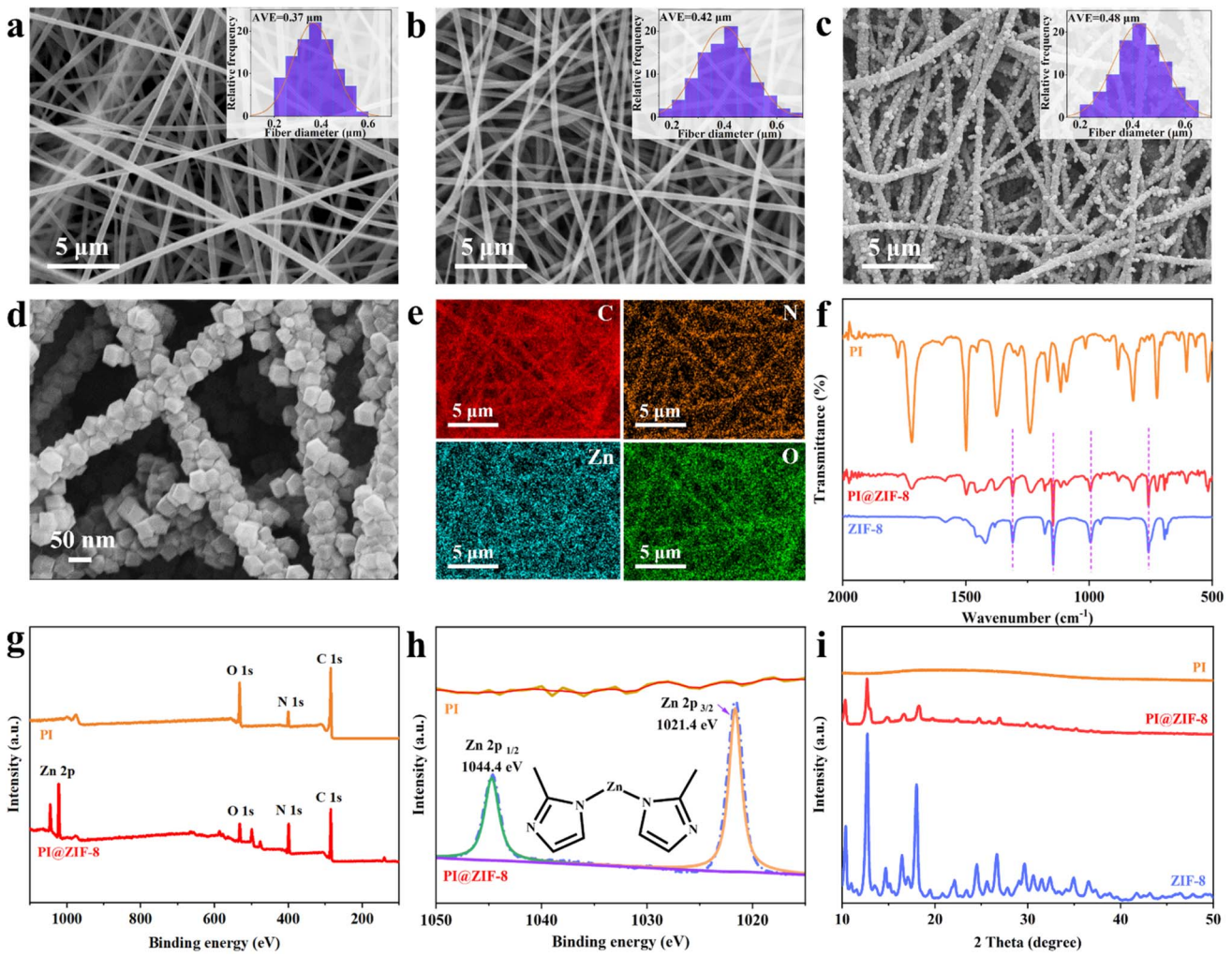

Fig. 2 Structural characterization studies of the constructed nanofiber separators with 3D multiscale MOF networks. (a–d) Surface morphologies of PAA, PI and PI@ZIF-8 nanofiber separators. (e) EDS mappings of the PI@ZIF-8 samples. (f) FTIR spectra of ZIF-8 nanounits, PI and PI@ZIF-8 separators. (g) Full XPS spectra and (h) high-resolution Zn 2p spectra of PI and PI@ZIF-8 nanofiber separators. (i) XRD patterns of ZIF-8 nanounits, PI and PI@ZIF-8 nanofiber separators.

photoelectron spectroscopy (XPS) in Fig. 2g, the spectrum of pristine PI separators merely exhibited the peaks of C 1s, N 1s and O 1s. After self-assembly of ZIF-8 nanounits, the observed new peaks for Zn $2p_{3/2}$ and Zn $2p_{1/2}$ also suggested the effective combination of ZIF-8 and PI, and the characteristic peak of Zn $2p_{3/2}$ centered at 1021.4 eV demonstrated the Zn(II) species encompassed with four N atoms (Fig. 2h).[36] Furthermore, the X-ray diffraction (XRD) pattern of PI@ZIF-8 nanofiber separators showed the clear characteristic peaks of ZIF-8 (Fig. 2i), indicating that the constructed multiscale MOF networks fulfilled high-quality crystal structures. The above results convincingly proved the great potential and feasibility for fabricating the nanofiber separators with 3D multiscale MOF networks through a surface-etching induced *in situ* self-assembly approach.

Mechanical properties are an important factor in evaluating whether the separators could ensure the safe operation of batteries. As shown in Fig. 3a, the pristine PI nanofiber separators exhibited a tensile strength of 22.7 MPa and breaking elongation of 66.5% derived from the dry stretching preparation. After the loading of ZIF-8, the obtained PI@ZIF-8 nanofiber separators displayed a slight reduction in mechanical strength (21.6 MPa) and breaking elongation (57.7%). After soaking in electrolyte for 24 h, the corresponding tensile strengths of PI and PI@ZIF-8 nanofiber separators still remained at 22.5 and 21.1 MPa with negligible changes, reflecting their long-term mechanical stability within electrolyte. Fig. 3b depicts the photographs of different samples followed by bending and folding treatments. The PI and PI@ZIF-8 nanofiber separators well restored the original appearance and maintained consistent flatness after testing, while PE separators produced a great deal of irreversible wrinkles. These test results suggested the superior mechanical flexibility of the 3D

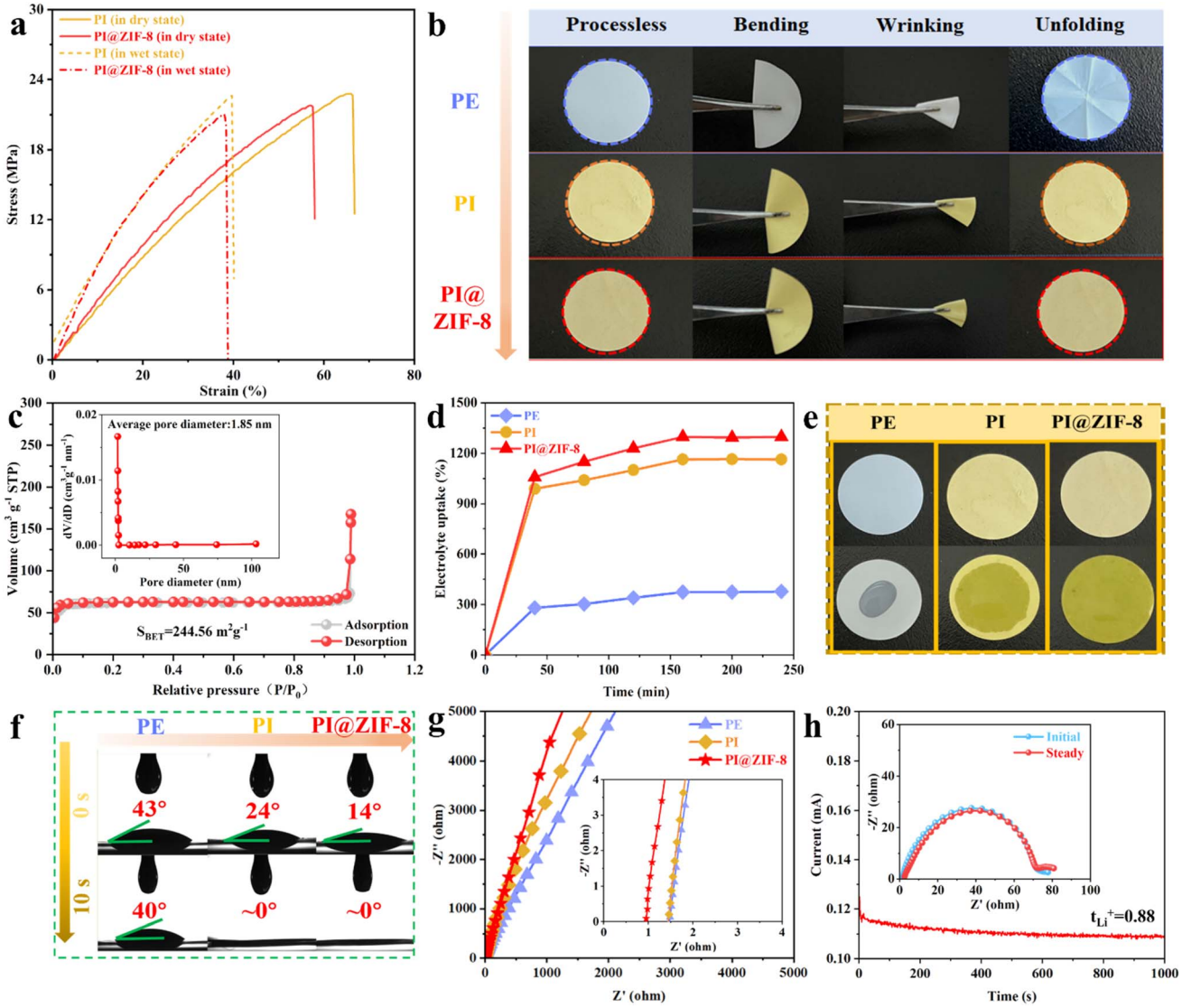

Fig. 3 (a) Stress–strain curves of PI and PI@ZIF-8 nanofiber separators. (b) Wrinkle tests of PE, PI and PI@ZIF-8 samples. (c) N_2 adsorption–desorption isotherms and pore size distribution of PI@ZIF-8 nanofiber separators. Electrolyte (d) uptakes, (e) dropping experiments and (f) contact angles of PE, PI and PI@ZIF-8 samples. (g) Impedance spectra of PE, PI and PI@ZIF-8 separators. (h) Current–time curves and the relevant Nyquist plots of PI@ZIF-8 nanofiber separators in symmetric Li–Li cells.

multiscale MOF networks, which were mainly attributed to the inherent robustness of the PI skeleton, as well as the strong binding interaction between PI nanofibers and ZIF-8 nanounits, thereby contributing to the continuous conduction of Li^+ and the valid inhibition of dendrite growth for higher safety.

The pore size distribution and specific surface area of the multiscale MOF networks were explored by N_2 adsorption–desorption testing. As displayed in Fig. 3c and S2,† the micro/mesoporous structure of PI@ZIF-8 samples was vindicated, since the tested curve presented an H_3 hysteresis loop and IV-type isotherm features.[42,43] Compared with PI samples (5.23 $m^2\ g^{-1}$), the PI@ZIF-8 nanofiber separators obtained a significant increase in specific surface area (244.56 $m^2\ g^{-1}$), mainly attributed to the ultra-high specific surface area of ZIF-8 (1038.34 $m^2\ g^{-1}$). Meanwhile, the PI@ZIF-8 and PI samples also showed much higher porosities than PE separators (Fig. S3†). Moreover, it was seen from Fig. 3d that the PI@ZIF-8 nanofiber separators delivered a superior electrolyte absorption rate of 1298%. When 20 μL of electrolyte was added dropwise to the middle of the three samples (Fig. 3e), only the PI@ZIF-8 nanofiber separators achieved rapid and complete infiltration and spreading and also obtained the highest electrolyte immersion height (Fig. S4†). In the electrolyte contact angles test (Fig. 3f), the PI@ZIF-8 nanofiber separators presented the minimum instantaneous contact angle. After 10 s, the contact angles of PI@ZIF-8 and PI separators quickly dropped to 0°, whereas the PE separators still retained a large contact angle of 40°. The test results could be mainly attributed to the PI@ZIF-8 nanofiber separators possessing the 3D porous and crosslinked network structure with large specific surface area and high porosity, which were instrumental in strengthening the electrolyte wettability and absorptivity. Overall, the 3D multiscale MOF networks were conducive to improving the electrolyte affinity for high ionic transport properties.[44]

The Nyquist curves in Fig. 3g were measured to characterize the ion conduction capability of the three separators, which demonstrated the lowest bulk resistance of PI@ZIF-8 samples. As shown in Table S1,† the ionic conductivity of PI@ZIF-8 nanofiber separators (2.40 mS cm^{-1}) was much higher than that of PE (0.65 mS cm^{-1}) and PI (1.65 mS cm^{-1}) separators. It was well-known that the Li^+ transference number (t_{Li^+}) was an important indicator to estimate the Li^+ mobility for separators. A larger t_{Li^+} implied a greater number of "free Li^+" and anchored anions, thereby homogenizing Li^+ deposition and avoiding Li dendrite formation.[45] The polarization curves and the impedance diagrams in the initial and steady states of the symmetric Li–Li cells are presented in Fig. 3h and S5.† The calculated t_{Li^+} value for PI@ZIF-8 nanofiber separators was 0.88, much higher than that of PE separators. The superior ionic conductivity and t_{Li^+} values confirmed the outstanding ion transport level of the nanofiber separators with 3D multiscale MOF networks, which could afford continuous Li^+ linear transmission channels at the micrometer scale, while sub-nano pores and Lewis acid sites within ZIF-8 nanounits could serve as ion sieves to selectively confine the movement of larger anions for accelerating the migration of more free Li^+.[46,47]

Study on Li^+ adsorption and the diffusion mechanisms for the 3D multiscale MOF networks was performed using DFT calculations from an atomic viewpoint. As shown in Fig. 4a, ZIF-8 featured both types of pore passageways to carry the migration motion of Li^+, including six 4-MRs and eight 6-MRs, which constructed 1D transmission pathways with apertures of 0.8 and 3.4 Å from multiple directions.[48,49] The four-coordinate clusters formed by the integration of Li^+ and organic solvent molecules acted as the main species,[50] so the de-solvation ability of the multiscale MOF networks was evaluated by calculating the adsorption energies of the two basic units within ZIF-8 on solvated clusters. The 4-MR units of ZIF-8 respectively exhibited adsorption energies of −4.13, −2.90, −2.38 and −2.42 eV for PF_6^- and the solvated clusters ($Li^+(EC)_4$, $Li^+(DMC)_4$ and $Li^+(EMC)_4$), which were much stronger than that of pure Li^+ (−0.93 eV) (Fig. 4b and S6†). It was worth noting that the adsorption energy for the 6-MR structure on Li^+ was positive (1.33 eV), suggesting an antipathy nature towards Li (Fig. 4d and S7†). The above results indicated that the diffusion channels within ZIF-8 could selectively transport Li^+, and the high-efficiency Li^+ migration was promoted based on the similarity between the channel diameter (0.8 Å) of 4-MR and the Li^+ diameter (0.76 Å). Moreover, the adsorption energies for solvent clusters by ZIF-8 were much higher than that for individual Li atoms, which was beneficial for increasing the surface Li^+ concentration and diffusion in 1D channels. In addition, the charge density differences in Fig. 4c–e displayed evident charge transfer for the 4-MR and 6-MR units interacting with $Li^+(EC)_4$, further validating the de-solvation action and ionic conduction function of the multiscale MOF networks. As a result, the PI@ZIF-8 nanofiber separators could alleviate the obstacles for Li^+ de-solvation and expedite the efficient conduction of Li^+/electrons following 1D pathways, thanks to the highly ordered multiscale MOF network structure.

Theoretically, the excellent mechanical stability, surficial electrolyte affinity and ionic conductivity were conducive to reinforcing the inhibition ability of separators for dendrite growth, which was evaluated through the Li plating/stripping behaviors within symmetrical Li||Li cells at different current densities. The Li||PE||Li cells delivered severely deteriorated polarization voltages within 211 h at 1.0 mA cm^{-2}, while a sharp polarization suddenly occurred for Li||PI||Li cells after 506 h, as shown in Fig. 5a. With the assistance of multiscale MOF networks, the Li||PI@ZIF-8||Li cells achieved highly stable cycling behavior over 2000 h with a minimum polarization voltage of 37.5 mV. Moreover, it was seen from Fig. 5b that the Li||PI@ZIF-8||Li cells exhibited much lower impedance values before and after cycling, indicating that the PI@ZIF-8 nanofiber separators effectively suppressed the Li dendrite formation and reinforced the electrode/electrolyte interface stability. Furthermore, the rate performance of Li||Li cells at various current densities from 0.5 to 2.5 mA cm^{-2} at an areal capacity of 1.0 mA h cm^{-2} is shown in Fig. 5c. Despite the continuous increase in current densities, the Li||PI@ZIF-8||Li cells still maintained an incredibly stable polarization vibration compared with Li||PE||Li and Li||PI||Li cells. More importantly, when cycled at a "higher current density" of 2.5 mA cm^{-2}

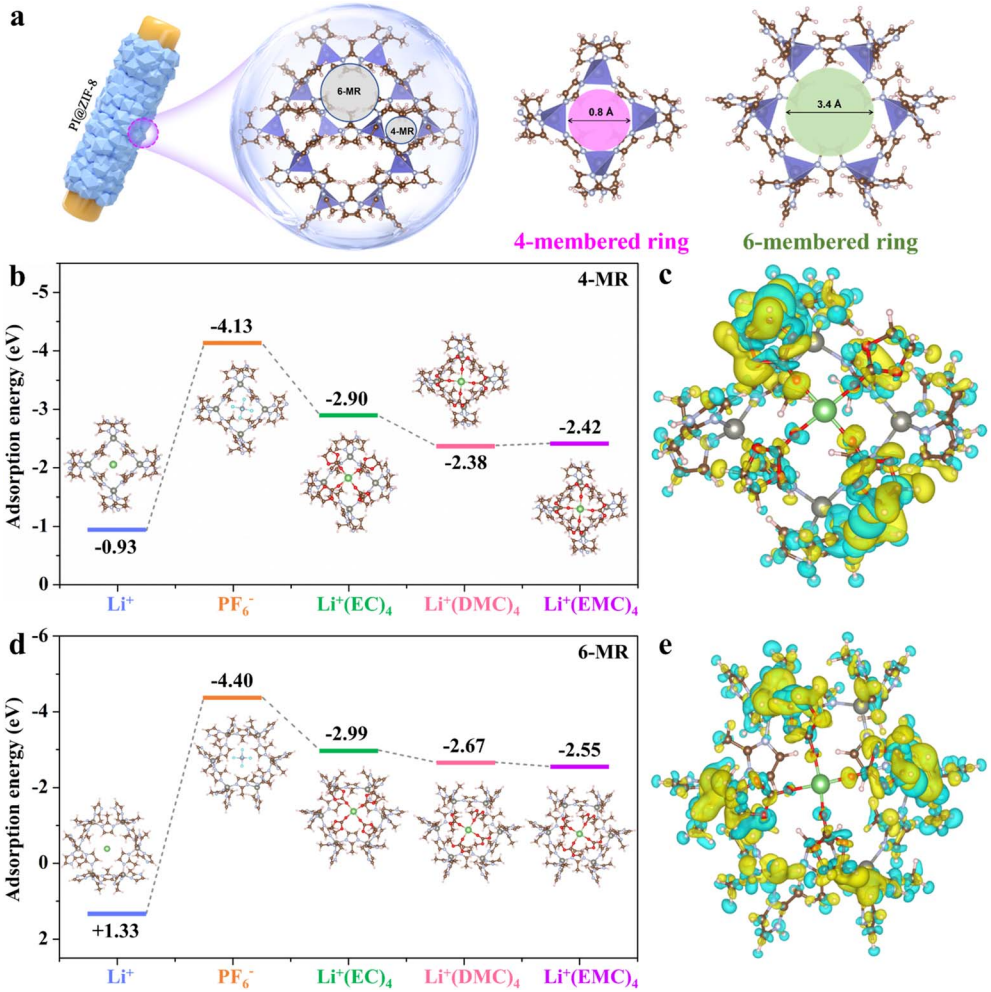

Fig. 4 (a) The atomic structure of ZIF-8 consisting of 4-MR units on faces and 6-MR units on body diagonals. Adsorption energies of (b) 4-MR and (d) 6-MR units for Li^+, PF_6^- and different solvated clusters. Charge density differences of (c) 4-MR and (e) 6-MR units interacting with $Li^+(EC)_4$, in which the cyan and yellow isosurfaces respectively represent the electron depletion and accumulation zones.

(Fig. S8a†) and "larger stripping/plating capacity" of 2.5 mA h cm^{-2} (Fig. S8b†), the Li||PI@ZIF-8||Li cells also displayed favorable long-term cycling stability, while the Li||PE||Li cells showed significant instability and short-circuit accidents during cycling, which could furnish the evidence for uniform Li nucleation and growth enabled by the PI@ZIF-8 nanofiber separators even at high current densities and large Li deposition amounts.

For further estimating the dendrite-suppressing capability of the three separators, the SEM images and digital photographs of Li electrodes disassembled from the Li||Li cells after rate capability testing were characterized. In contrast to the flat and dense Li surface without dendritic morphology in Li||PI@ZIF-8||Li cells (Fig. 5g), the Li||PE||Li and Li||PI||Li cells displayed the porous and loose Li deposition morphologies accumulated with generous "dead Li" to varying degrees (Fig. 5d and S9a†). Meanwhile, the cross-sectional views of the Li anodes within Li||PE||Li and Li||PI||Li cells showed the much thicker Li deposition layers with rough and disruptive morphologic structures (Fig. 5e and S9b†). This was primarily because of the detrimental interface affinity and ion-conducting properties of PE and PI separators, provoking uneven Li deposition and unfavorable interfacial polarization.[9] Conversely, the thin and compact Li deposition layers with distinct SEI films were observed from the Li anode of Li||PI@ZIF-8||Li cells (Fig. 5h), signifying the effective obstruction for Li dendrite formation and the significant promotion for SEI stabilization assisted by the 3D multiscale MOF networks. By comparing the surface morphologies of separators after cycling, it was found that the pores of PE separators were almost completely blocked (Fig. 5f), while a large amount of by-products had accumulated on the surface of PI separators (Fig. S9c†). In sharp contrast, the PI@ZIF-8 nanofiber separators well retained the highly stable 3D porous network structure without obvious loss of ZIF-8 nanounits (Fig. 5i), which validated the strong bonding between ZIF-8 and the PI skeleton that could satisfy the long-term cycling requirements. At the same time, the XRD patterns of the PI@ZIF-8 nanofiber separators after cycling still maintained the significant characteristic peaks of ZIF-8 (Fig. S10†), further demonstrating their stability during cycling. XPS was conducted to identify the chemical compositions of the formed SEI film on the cycled Li surface. The

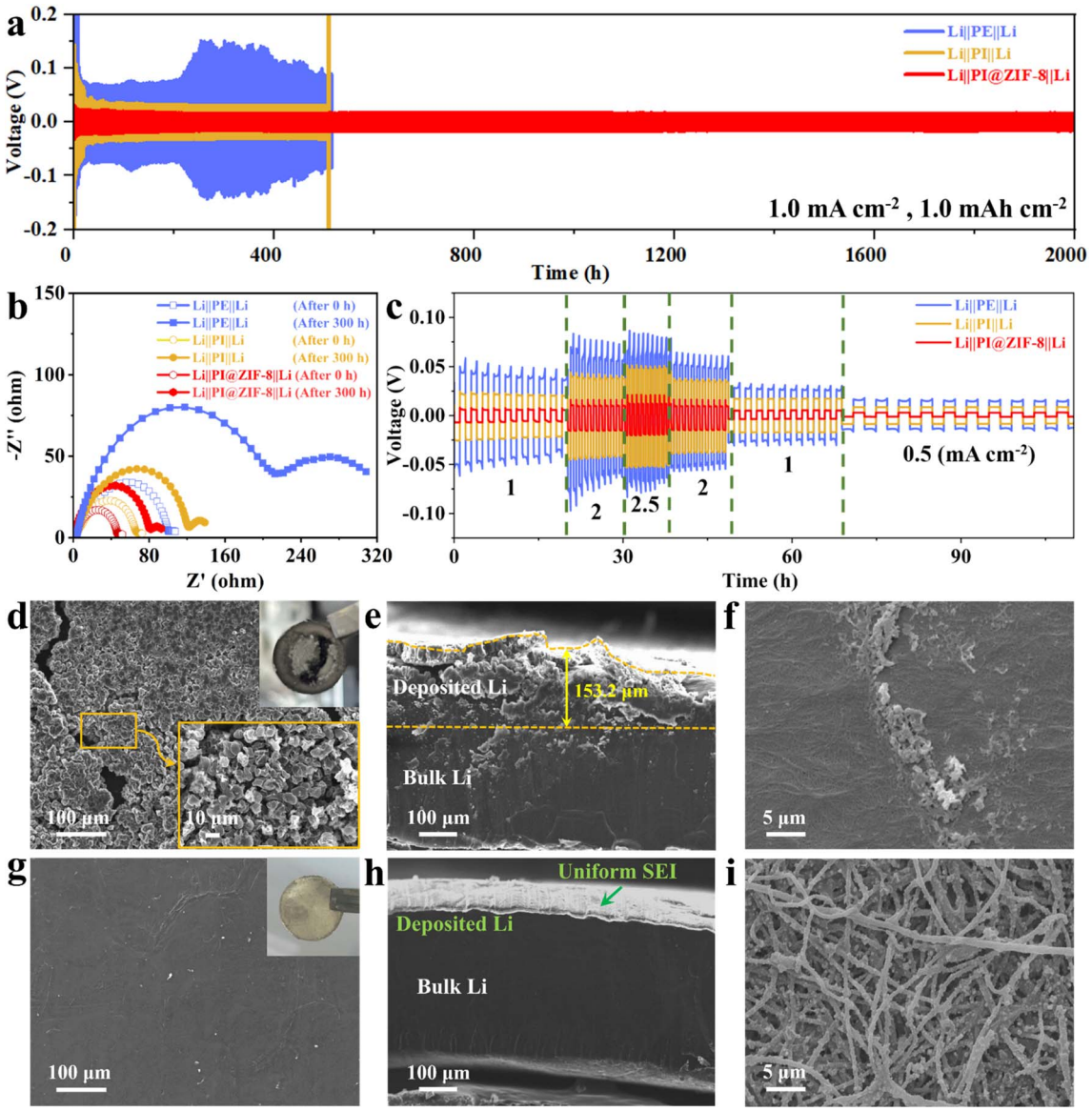

Fig. 5 Li plating/stripping behaviors within symmetric Li||Li cells with different separators. (a) Cycling performance of Li||Li cells at a current density of 1.0 mA cm^{-2} with an areal capacity of 1.0 mA h cm^{-2}. (b) Electrochemical impedances of Li||Li cells before and after cycling. (c) Rate performance of Li||Li cells at increased current densities from 1.0 to 2.5 mA cm^{-2} with an areal capacity of 1.0 mA h cm^{-2}. Digital photographs and SEM images of the detached Li electrodes and separators from the (d–f) Li||PE||Li and (g–i) Li||PI@ZIF-8||Li cells after cycling.

appearance peaks relevant to LiF were observed in F 1s (Fig. S11a†) and Li 1s spectra (Fig. S11b†), which had high Young's modulus and acted as favorable SEI constituents, playing an important role in protecting the SEI film from volume expansion and alloying reactions.[51] In the Zn 2p spectrum for the cycled PI@ZIF-8 separators (Fig. S11c†), the intactly appearing Zn metal centers proved the admirable structural stability of ZIF-8 nanounits during cycling. Compared to the peak positions before cycling (Fig. 2h), the two peaks within the Zn 2p spectrum mildly shifted towards higher binding energies, which well demonstrated that the Zn sites of ZIF-8 could interact with some anions within electrolyte, thereby accelerating the Li^+ mobility.[52]

To better evaluate the positive role of PI@ZIF-8 nanofiber separators in the regulation of Li deposition behaviors, the morphologies of Li deposits within Li||Cu cells were investigated under different deposition conditions. Due to the inevitable roughness of the electrode surface, the electric field distribution near the surface was uneven. In the case of PE separators, the charges accumulated at the tip and directed Li^+ to preferentially deposit at the tip (Fig. 6a), which induced the accelerated vertical growth of deposited Li instead of flat growth, ultimately resulting in the formation of Li dendrites. In complete contrast, Li^+ could be uniformly redistributed when passing through the PI@ZIF-8 nanofiber separators, which could effectively prevent Li^+ from accumulating at the tip and achieve homogeneous distribution at the molecular level (Fig. 6b). As presented in Fig. 6c, Li nuclei with homogeneously spherical structures were well-distributed on the surface of Cu foil under a small Li deposition amount of 0.5 mA h cm^{-2}.

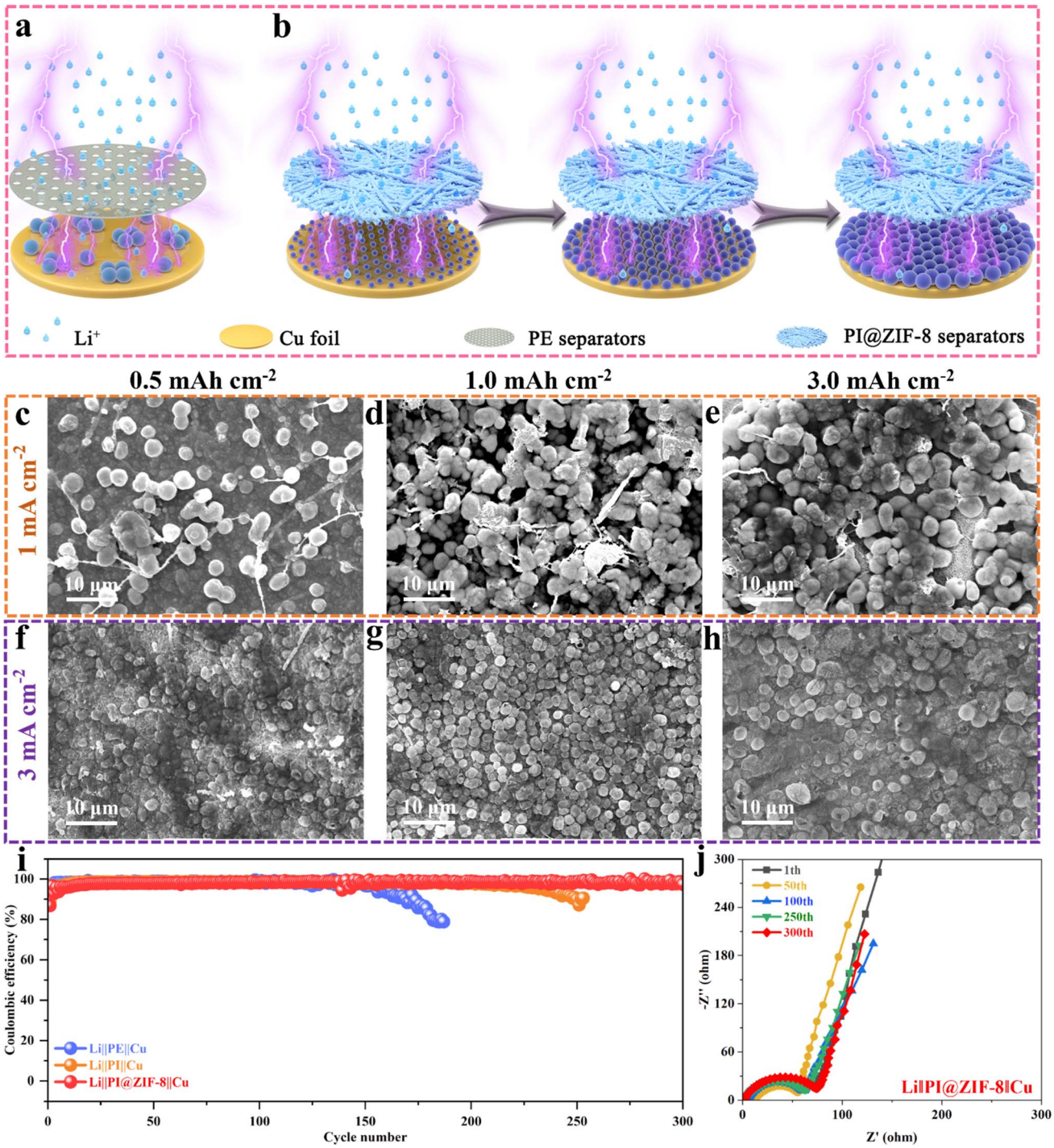

Fig. 6 Electrochemical Li plating/stripping behaviors within the Li||Cu cells with different separators. Schematics showing Li deposition on Cu foil with (a) PE and (b) PI@ZIF-8 separators. SEM images of Li deposits on Cu foil within Li||PI@ZIF-8||Cu cells discharged at (c–e) 1.0 mA cm^{-2} and (f–h) 3.0 mA cm^{-2}. (i) CEs of Li plating/stripping for the three Li||Cu cells at 0.5 mA cm^{-2} and 1.0 mA h cm^{-2}. (j) Electrochemical impedances of Li||PI@ZIF-8||Cu cells after cycling.

When 1.0 mA h cm^{-2} of Li was plated, the closely packed ellipsoidal Li nuclei were still observed (Fig. 6d). Even after increasing the Li deposition capacity to 3.0 mA h cm^{-2}, the spherical structure was still visible and the diameter of the Li nucleus maintained slow growth without Li dendrites being generated on Cu foil (Fig. 6e). As the current density increased from 1.0 to 3.0 mA cm^{-2}, the ellipsoidal particles with smaller size on Cu foil overlapped and were stacked together, displaying flat and dendrite-free morphologies (Fig. 6f–h). As compared, the Li^+ deposition track within Li||PE||Cu cells was affected by the uneven electric field on the electrode surface, and the irregular island-like and wire-like Li nuclei were shown on the

surface of Cu foil (Fig. S12†). The messy Li deposits turned to aggravate the uneven electric field and induce uncontrollable dendritic growth.[53] Significantly, this striking contrast firmly demonstrated that the PI@ZIF-8 nanofiber separators with 3D multiscale MOF networks could effectively guide uniform Li nucleation.

Moreover, the electrochemical Li plating/stripping behaviors for the three separators in Li‖Cu half-cells were investigated at 0.5 mA cm^{-2} and 1.0 mA h cm^{-2}. As shown in Fig. 6i, the CEs of Li‖PE‖Cu cells suffered from a thorough decay after 150 cycles, while a fast decline of CEs for Li‖PI‖Cu cells after 220 cycles was observed, indicating the constant breakage and reformation of SEI films. On the contrast, steady CEs were obtained using Li‖PI@ZIF-8‖Cu cells upon 300 cycles, which was far superior to Li‖PE‖Cu and Li‖PI‖Cu cells. Through the evolution of battery impedances over varying cycle numbers (Fig. 6j and S13†), the Li‖PI@ZIF-8‖Cu cells consistently maintained the lowest impedances at different cycles. Even when the cycle number increased to 300, the impedance value stabilized at around 77 Ω, mainly due to the survival from insulated "dead Li".[54] In addition, the voltage–capacity curves of the initial Li deposition process for the three samples are presented in Fig. S14.† The nucleation overpotential of Li‖PI@ZIF-8‖Cu cells was much lower than that of Li‖PE‖Cu and Li‖PI‖Cu cells, suggesting that the 3D multiscale MOF networks effectively improved the lithiophilicity of the electrode surface and reduced the Li nucleation overpotential on the Cu surface. Furthermore, the corresponding polarization profiles for the assembled Li‖Cu cells were analyzed to reflex the difficulty level of Li plating/stripping. The voltage polarizations of Li‖PE‖Cu and Li‖PI‖Cu cells first decreased and then increased during cycling (Fig. S15a and b†), which demonstrated a gradual stabilization of the electrode–electrolyte interface until later deterioration. In contrast, the Li‖PI@ZIF-8‖Cu cells possessed lower voltage polarizations and remained constant over time (Fig. S15c†), indicating few obstacles for the heterogeneous nucleation and Li growth.[55]

Subsequently, the potential application of PI@ZIF-8 nanofiber separators was investigated in the LMBs by coupling with $LiFePO_4$ (LFP) as the cathode. It was found from Fig. 7a that all assembled LFP‖Li cells had only one pair of redox peaks in the tested CV curves. The LFP‖PI@ZIF-8‖Li cells delivered higher-intensity oxidation and reduction peaks than the other two samples, well confirming the improved electrochemical reaction kinetics of the PI@ZIF-8 nanofiber separators.[56] The rate performance of LFP‖Li cells with the three separators was compared as shown in Fig. 7b. In contrast with LFP‖PE‖Li and LFP‖PI‖Li cells, the advantage in discharge capacity was more pronounced for LFP‖PI@ZIF-8‖Li cells, especially under high-rate conditions. When recovering from a high-rate of 5.0C to the initial low-rate of 0.2C, the LFP‖PI@ZIF-8‖Li cells also presented good capacity reversibility, suggesting outstanding electrochemical stability even at high current densities. This superior rate capability was mainly due to the well-constructed 3D multiscale MOF networks, which could supply long-distance and continuous transport channels for Li^+, thereby realizing rapid Li^+ transmission in battery systems.

The long-term cycling stability of LFP‖Li cells was regarded as another important criterion to evaluate the applicability of PI@ZIF-8 nanofiber separators. As shown in Fig. 7c, the LFP‖PE‖Li and LFP‖PI‖Li cells were infeasible for long-life energy devices, which delivered relatively fast capacity attenuation at 1.0C. Prominently, the LFP‖PI@ZIF-8‖Li cells achieved a high capacity retention rate of 97.4% after 300 cycles and also obtained the desired cycling stability with higher CEs and discharge capacities during 800 cycles at 2.0C (Fig. S16†). More significantly, the relevant reports summarized in Table S2† further demonstrated the outstanding electrochemical performance of the batteries using the PI@ZIF-8 nanofiber separators, which were competitive with previously reported nanofiber separators. When matched with the high-loading LFP cathodes (~4.5 mg cm^{-2}), it was seen from Fig. S17† that the LFP‖PI@ZIF-8‖Li cells still exhibited superior cycling stability with a much higher capacity retention rate of 95.4% after 240 cycles in comparison with the LFP‖PE‖Li cells. In addition, the impedance values of the LFP‖PI@ZIF-8‖Li cells before and after cycling were much lower than those of the other two samples (Fig. 7d). After 300 cycles, the LFP‖PI@ZIF-8‖Li cells presented slight impedance changes thanks to the compatible electrode/electrolyte interface stability, while serious deterioration was observed from the interfacial resistances of LFP‖PE‖Li and LFP‖PI‖Li cells. It was seen from the SEM images in Fig. S18a–c† that the Li surface detached from the cycled LFP‖PI@ZIF-8‖Li cells was smooth and compact, whereas the Li anodes for LFP‖PE‖Li and LFP‖PI‖Li cells showed quite rough surfaces accompanied by Li dendrite growth and "dead Li" accumulation. Moreover, the cross-section views in Fig. S18d–f† showed a damaged loose structure with numerous cracks and thick deposition layers within LFP‖PE‖Li and LFP‖PI‖Li cells, while flat and dense deposited Li equipped with a uniform SEI film was attained using the LFP‖PI@ZIF-8‖Li cells. Besides, the PI@ZIF-8 nanofiber separators still preserved their original 3D porous crosslinked network structure without the abscission of ZIF-8, unlike the varying hole-blockade extents within PE and PI separators (Fig. S18g–i†), which verified the excellent structural stability of PI@ZIF-8 nanofiber separators to guarantee high-efficiency Li^+ transport during the cycling process.

In addition, the linear sweep voltammetry (LSV) experiments (Fig. 7e) revealed the superior anodic stability of PI@ZIF-8 nanofiber separators with a relatively high decomposition voltage, reflecting the novel configuration of the multiscale MOF networks and improved electrochemical robustness and operating voltage range, which was closely related to high specific surface area and good electrolyte absorption.[57] NCM811‖Li cells were assembled to explore the applicability of PI@ZIF-8 nanofiber separators for high-voltage cathode materials. When cycled at 0.5C (Fig. 7f), the NCM811‖PE‖Li cells experienced severe capacity degradation with sharp polarization voltage fluctuations (Fig. S19a†), but the NCM811‖PI@ZIF-8‖Li cells exhibited admirable electrochemical stability with a high capacity retention of 94.5% after 250 cycles, meaning a decay rate of 0.022% per cycle. From the charge–discharge curves of NCM811‖PI@ZIF-8‖Li cells at different cycles as shown in Fig. S19b,† it was seen that the discharge capacity slightly

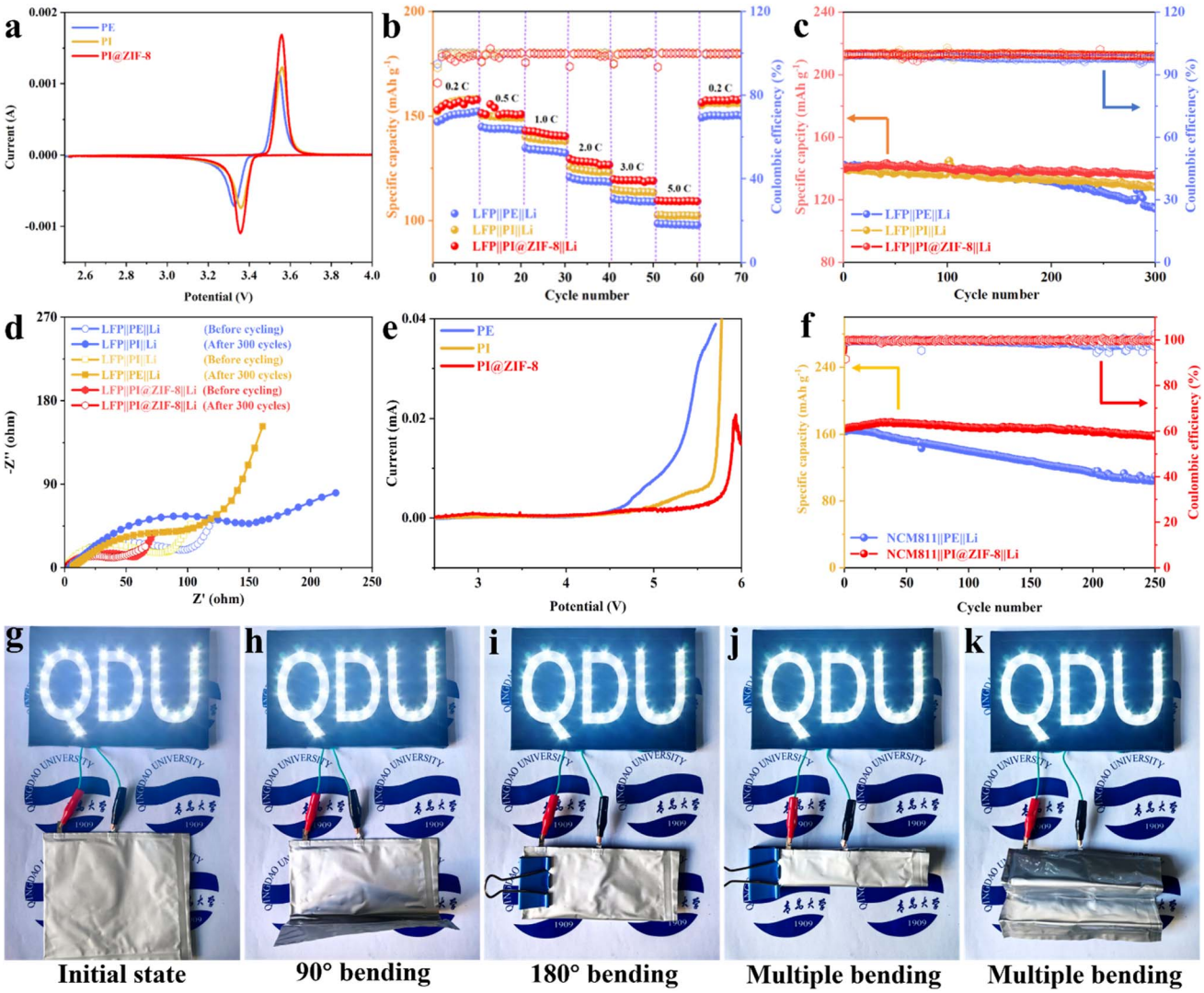

Fig. 7 Electrochemical properties of the LMBs with different separators. (a) Cyclic voltammograms, (b) rate performance, (c) long-term cycle performance at 1.0C, and (d) electrochemical impedances before and after cycling of LFP||PE||Li, LFP||PI||Li and LFP||PI@ZIF-8||Li cells. (e) LSV curves of the three separators. (f) Cycling performance of NCM811||Li cells at 0.5C. Photos of LFP||PI@ZIF-8||Li pouch cells showing well-running at (g) initial state, (h) 90° bending, (i) 180° bending and (j and k) multiple bending states.

declined with negligible polarization along with the increased cycles, proving the great potential of the PI@ZIF-8 nanofiber separators for the field of high-voltage batteries. Furthermore, the flexibility and safety aspects of PI@ZIF-8 nanofiber separators were analyzed by testing the pouch cells under extreme conditions. The LFP||PI@ZIF-8||Li pouch cells were fabricated and fully charged to power light-emitting diodes, as shown in Fig. 7g. The light emission remained intact even in various folded states from 90° to 180° and under multiple bending conditions (Fig. 7h–k), suggesting the reliability and high-security of these nanofiber separators with 3D multiscale MOF networks towards advanced LMBs.

Thermal stability was one of the important indicators to assess the safety of separators, which really mattered for the practical use of LMBs.[58] Fig. 8a shows the instantaneous heat resistance of the three separators based on the combustion tests. The PE separators underwent distinct thermal contraction after 5 s, while there was no significant change in external dimensions of PI and PI@ZIF-8 nanofiber separators even after being heated for 30 s. Once placed within the flame, the PI and PI@ZIF-8 nanofiber separators exhibited certain self-extinguishing characteristic with the reserved partial residues, but PE separators were immediately ignited and burned to ashes (Fig. 8b). Combined with the differential scanning calorimetry (DSC) measurement in Fig. 8c, both the PI and PI@ZIF-8 nanofiber separators showed no obvious endothermic peak below 280 °C, indicating their superior thermostability that resulted from the PI macromolecule backbone composed of aromatic benzene rings and heterocyclic imide rings.[59] While for the PE separators, an endothermic peak at ~145 °C corresponding to their melting point emerged.[60] The infrared radiation thermographic photographs (Fig. 8d) and the dimensional changes (Fig. 8e) of all separators from 100 to 200 °C were further characterized. In striking contrast to the severe

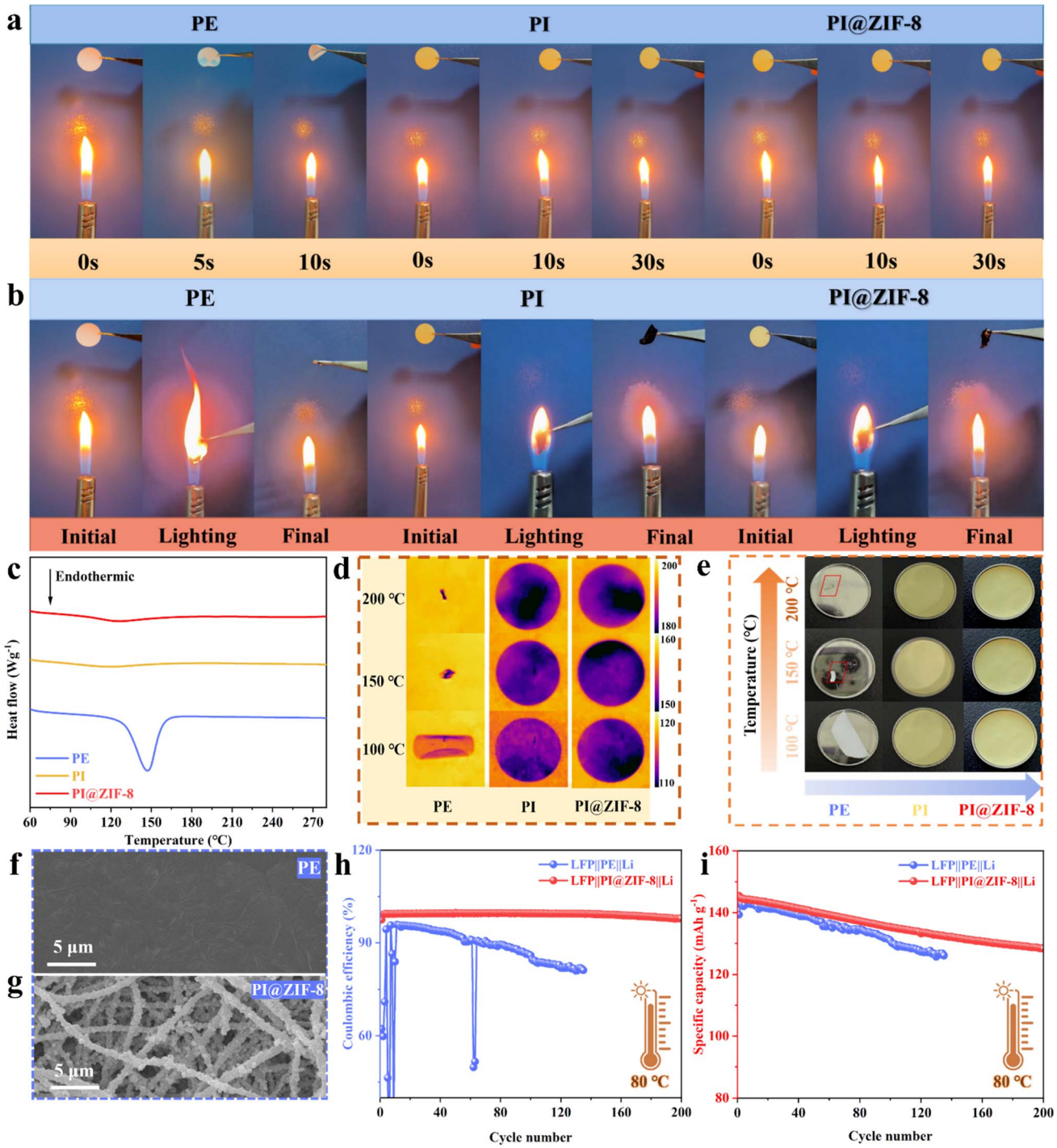

Fig. 8 Thermal stability analyses of the three separators and their electrochemical behaviors under high-temperature conditions. (a) Instantaneous heat resistance and (b) flammability test based on the combustion tests. (c) DSC curves, (d) infrared radiation thermographic photographs and (e) thermal shrinkage photographs of the three separators from 100 to 200 °C. SEM images of (f) PE and (g) PI@ZIF-8 separators after heat-treatment. Cycling performance of the LFP||Li cells at 1.0C for 200 cycles at 80 °C: (h) CEs and (i) specific capacities.

deformation and melting of PE separators, the PI and PI@ZIF-8 nanofiber separators displayed excellent thermal dimensional stability. In addition, the molten PE separators had become the nonporous "dead film" (Fig. 8f), but the PI and PI@ZIF-8 nanofiber separators after heat-treatment still fulfilled intact 3D porous configuration (Fig. 8g), which could avoid the short-circuit accidents of LMBs at elevated temperatures. In view of this, the assembled LFP||Li cells were executed at 80 °C to detect the electrochemical behaviors. As shown in Fig. 8h and i, the LFP||PI@ZIF-8||Li cells delivered much better cycling stability and longer life-span accompanied by higher CEs and discharge capacities as compared to the LFP||PE||Li cells, implying that

the highly porous interlaced PI@ZIF-8 nanofiber separators did not largely decrease the ion transport and possess good compatibility with current commercial LFP cathodes even under elevated-temperature operating conditions.

3. Conclusion

In summary, a thermomechanically stable nanofiber separator with 3D multiscale MOF networks was designed and synthesized for LMBs through a promising electrospinning-assisted *in situ* self-assembly strategy. This unique structure was achieved by constructing well-ordered ZIF-8 nanounits along 1D PI nanofibers to provide continuous Li^+ linear pathways at the micrometer scale, and the formed 1D MOF nanofibers were interconnected to generate a monolithic 3D network for high-efficiency Li^+ transport in the bulk of separators. The resulting PI@ZIF-8 nanofiber separators with 3D multiscale MOF networks delivered a superior Li^+ transference number of 0.88, high ionic conductivity of 2.40 mS cm^{-1} and wide electrochemical window of 4.8 V, coupled with excellent electrolyte affinity, good thermostability and strong mechanical stability. The Li||PI@ZIF-8||Li cells stably worked for over 2000 h without short-circuit accidents, indicating that the PI@ZIF-8 nanofiber separators significantly restrained Li dendrite formation and strengthened SEI robustness to guarantee the electrode/electrolyte interface stability. Moreover, the assembled Li||PI@ZIF-8||Cu cells also performed well, which further confirmed the effective regulation of Li deposition behaviors through the multiscale MOF networks. Besides, the desired long-term cycling durability with higher CEs and discharge capacities was achieved using LFP||PI@ZIF-8||Li cells, even under high-rate or high-temperature conditions. The ingenious design of these high ion-transmitting and high-safety nanofiber separators with 3D multiscale MOF networks presented a research avenue with significant potential for the future commercialization of high-energy-density LMBs.

Data availability

The data supporting this article have been included as part of the ESI.† More data can be provided upon request.

Conflicts of interest

The authors declare no conflict of interest.

Acknowledgements

This work was supported by the National Natural Science Foundation of China (grant number 22475021, 22179010 and 21973008), Shandong Provincial Natural Science Foundation of China (ZR2024QE041) and Natural Science Foundation of Qingdao of China (24-4-4-zrjj-60-jch). We would like to appreciate Shiyanjia Lab (**https://www.shiyanjia.com**) for first-principles calculation.

References

1 Y. S. Qian, K. Chen, Z. X. Feng, Y. Ouyang, Q. Q. Lan, C. Zhang, W. Feng, Y. E. Miao and T. X. Liu, *Small Struct.*, 2023, **4**, 2200383.
2 Y. C. Pang, M. Guan, Y. L. Pan, M. Tian, K. Huang, C. Z. Jiang, A. Xiang, X. Q. Wang, Y. J. Gong, Y. Xiang and X. K. Zhang, *Small*, 2022, **18**, 2104832.
3 S. J. Zheng, L. L. Mo, K. Chen, A. L. Chen, X. Zhang, X. S. Fan, F. L. Lai, Q. C. Wei, Y. E. Miao, T. X. Liu and Y. Yu, *Adv. Funct. Mater.*, 2022, **32**, 2201430.
4 J. Lee, H. J. Song, K. A. Min, Q. Y. Guo, D. K. Kim, Z. J. Zheng, B. C. Han, Y. J. Jung and L. Y. S. Lee, *Small Methods*, 2021, **5**, 2100215.
5 S. J. Zheng, Y. Y. Chen, K. Chen, S. Y. Yang, R. Bagherzadeh, Y. E. Miao and T. X. Liu, *J. Mater. Chem. A*, 2022, **10**, 19641–19648.
6 H. Kwon, J. Baek and H. T. Kim, *Energy Storage Mater.*, 2023, **55**, 708–726.
7 H. J. Zhao, G. D. Zhao, F. Q. Liu, T. Q. Xiang, J. J. Zhou and L. Li, *J. Colloid Interface Sci.*, 2024, **666**, 131–140.
8 X. R. Chen, B. C. Zhao, C. Yan and Q. Zhang, *Adv. Mater.*, 2021, **33**, 2004128.
9 X. X. Zhang, Q. M. Su, G. H. Du, B. S. Xu, S. Wang, Z. Chen, L. M. Wang, W. H. Huang and H. Pang, *Angew. Chem., Int. Ed.*, 2023, **135**, e202304947.
10 M. Guo, H. Y. Zhu, P. F. Wan, F. Xu, C. H. Wang, S. J. Lu, Y. F. Zhang, H. S. Fan and J. Xu, *Adv. Fiber Mater.*, 2022, **4**, 1511.
11 W. C. Ren, Y. N. Zheng, Z. H. Cui, Y. S. Tao, B. X. Li and W. T. Wang, *Energy Storage Mater.*, 2021, **35**, 157.
12 L. Yue, Z. Wang, D. Wang, W. Song, Z. Wu, W. Zhao, L. Zhang, Y. Luo, S. Sun, D. Zheng, B. Zhong, J. Zhao, Q. Liu, A. M. Asiri, X. Guo and X. Sun, *J. Mater. Chem. A*, 2022, **10**, 21149–21160.
13 J. Wang, Y. Liu, Q. Cai, A. Dong, D. Yang and D. Zhao, *Adv. Mater.*, 2022, **34**, 2107957.
14 B. He, S. Wu, Q. Zhao, Y. Meng, X. Tang, S. Yu, L. Yang, Y. Xu, T. Gao and D. Xiao, *J. Colloid Interface Sci.*, 2023, **629**, 1003–1014.
15 Q. Zhao, X. L. Wu, S. H. Li, Q. T. Zheng, S. Jiang, Y. Xu, B. He, L. Ma, Y. T. Luo, Y. J. Wang, W. L. Cen, Y. Meng and D. Xiao, *Small*, 2023, **19**, 2300378.
16 J. H. Deng, D. Q. Cao, X. Q. Yang and G. Q. Zhang, *Chem. Eng. J.*, 2022, **433**, 133934.
17 Y. Huang, S. J. Liu, Q. J. Chen, K. J. Jiao, B. Ding and J. H. Yan, *Adv. Funct. Mater.*, 2022, **32**, 2201496.
18 K. F. Liu, C. Y. Yang, X. G. Li, N. X. Dong, B. X. Liu, G. F. Tian, S. L. Qi and D. Z. Wu, *Energy Technol.*, 2022, **10**, 2100982.
19 J. C. Song, M. H. Ryou, B. Son, J. N. Lee, D. J. Lee, Y. M. Lee, J. W. Choi and J. K. Park, *Electrochim. Acta*, 2012, **85**, 524–530.
20 C. T. Hsieh, S. C. Lin, C. H. Lee, C. F. Liu and C. C. Hu, *J. Electrochem. Soc.*, 2019, **166**, A3132–A3138.
21 J. Y. Tan, L. Y. Kong, Z. M. Qiu and Y. R. Yan, *J. Solid State Electrochem.*, 2018, **22**, 3363–3373.

22 Y. Shimizu and K. Kanamura, *J. Electrochem. Soc.*, 2019, **166**, A754–A761.
23 M. Venkatesan, L. Veeramuthu, F. C. Liang, W. C. Chen, C. J. Cho, C. W. Chen, J. Y. Chen, Y. Yan, S. H. Chang and C. C. Kuo, *Chem. Eng. J.*, 2020, **397**, 125431.
24 M. Venkatesan, W. C. Chen, C. J. Cho, L. Veeramuthu, L. G. Chen, K. Y. Li, M. L. Tsai, Y. C. Lai, W. Y. Lee, W. C. Chen and C. C. Kuo, *Chem. Eng. J.*, 2022, **433**, 133620.
25 J. L. Xu, L. Yuan, G. Z. Liang and A. J. Gu, *J. Appl. Polym. Sci.*, 2021, **138**, e51233.
26 W. U. Arifeen, J. Choi, K. Yoo, J. Shim and T. J. Ko, *Chem. Eng. J.*, 2021, **417**, 128075.
27 M. L. Li, L. Sheng, R. Xu, Y. Yang, Y. Z. Bai, S. J. Song, G. J. Liu, T. Wang, X. L. Huang and J. P. He, *Compos. Commun.*, 2021, **24**, 100607.
28 J. W. Liu, J. N. Wang, L. Zhu, X. Chen, G. Yi, Q. Y. Ma, S. Y. Sun, N. Wang, X. M. Cui, Q. Q. Chai, J. T. Feng and W. Yan, *J. Mater. Chem. A*, 2022, **10**, 14098–14110.
29 G. D. Zhao, Z. L. Li, B. W. Cheng, X. P. Zhuang and T. Lin, *Sep. Purif. Technol.*, 2023, **315**, 123754.
30 H. J. Zhao, L. H. Zhang, S. J. Chen, X. P. Zhuang and G. D. Zhao, *J. Colloid Interface Sci.*, 2024, **674**, 537–546.
31 Z. Chang, H. Yang, A. Pan, P. He and H. Zhou, *Nat. Commun.*, 2022, **13**, 6788.
32 L. L. Du, B. Zhang, C. Yang, L. M. Cui, L. Q. Mai and L. Xu, *Energy Storage Mater.*, 2023, **61**, 102914.
33 D. Li, J. Wang, S. Guo, Y. Xiao, Q. Zeng, W. He, L. Gan, Q. Zhang and S. Huang, *Adv. Funct. Mater.*, 2022, **30**, 2003945.
34 S. B. Luo, N. P. Deng, H. Wang, Q. Zeng, Y. N. Li, W. M. Kang and B. W. Cheng, *Chem. Eng. J.*, 2023, **474**, 145683.
35 W. Y. Shi, J. Q. Shen, L. Shen, W. Hu, P. C. Xu, J. A. Baucom, S. X. Ma, S. X. Yang, X. M. Chen and Y. F. Lu, *Nano Lett.*, 2020, **20**, 5435.
36 L. L. Du, B. Zhang, W. Deng, Y. Cheng, L. Xu and L. Q. Mai, *Adv. Energy Mater.*, 2022, **12**, 2200501.
37 R. F. Lin, Y. M. Jin, X. B. Zhang, Y. M. Li, Y. Zhang and Y. P. Xiong, *Chem. Eng. J.*, 2024, **479**, 147558.
38 J. M. Yu, T. L. Guo, C. Wang, Z. H. Shen, X. Y. Dong, S. H. Li, H. G. Zhang and Z. D. Lu, *Nano Lett.*, 2021, **21**, 5805.
39 D. Ai, H. Li, Y. Zhou, L. L. Ren, Z. B. Han, B. Yao, W. Zhou, L. Zhao, J. M. Xu and Q. Wang, *Adv. Energy Mater.*, 2020, **10**, 1903881.
40 K. Akamatsu, S. Ikeda, H. Nawafune and S. Deki, *Chem. Mater.*, 2003, **15**, 2488–2491.
41 C. Luo, X. Wang, J. Wang and K. Pan, *Compos. Sci. Technol.*, 2016, **133**, 97–103.
42 L. Zhu, J. Wang, J. Liu, X. Chen, Z. Xu, Q. Ma, Z. Wang, J. Liang, S. Li and W. Yan, *Appl. Surf. Sci.*, 2022, **590**, 153085.
43 H. J. Zhao, F. F. Lan, H. Wang, S. J. Chen, G. D. Zhao, T. Lin and X. P. Zhuang, *Chem. Eng. J.*, 2024, **498**, 155177.
44 J. Wang, J. Liu, Q. Ma, X. Chen, S. Sun, H. Xu, L. Zhu, Z. Wang, J. Feng and W. J. Yan, *J. Alloys Compd.*, 2022, **899**, 163298.
45 X. X. Gao, L. Sheng, L. Yang, X. Xie, D. T. Li, Y. Gong, M. Cao, Y. Z. Bai, H. Y. Dong, G. J. Liu, T. Wang, X. L. Huang and J. P. He, *J. Colloid Interface Sci.*, 2023, **636**, 317–327.
46 D. M. Driscoll, S. N. Lavan, M. Zorko, P. C. Redfern, S. Ilic, G. Agarwal, T. T. Fister, R. S. Assary, L. Cheng, D. Strmcnik, M. Balasubramanian and J. G. Connell, *Chem*, 2023, **9**, 1955–1971.
47 T. Jiang, P. He, G. Wang, Y. Shen, C. Nan and L. Fan, *Adv. Energy Mater.*, 2020, **10**, 1903376.
48 C. L. Hobday, C. H. Woodall, M. J. Lennox, M. Frost, K. Kamenev, T. Düren, C. A. Morrison and S. A. Moggach, *Nat. Commun.*, 2018, **9**, 1429.
49 D. M. Zhang, R. N. Yang, J. H. Zhou, W. P. Liu, H. Q. Qin, Z. J. Zhang, X. X. Lei, A. J. Lu, Z. X. Mo, L. Miao and F. Dang, *Energy Storage Mater.*, 2023, **63**, 102976.
50 B. Jiang, V. Ponnuchamy, Y. Shen, X. Yang, K. Yuan, V. Vetere, S. Mossa, I. Skarmoutsos, Y. Zhang and J. Zheng, *J. Phys. Chem. Lett.*, 2016, **7**, 3554–3559.
51 S. Liu, X. Ji, J. Yue, S. Hou, P. Wang, C. Cui, J. Chen, B. Shao, J. Li, F. Han, J. Tu and C. Wang, *J. Am. Chem. Soc.*, 2020, **142**, 2438–2447.
52 C. Gao, Z. Jiang, S. Qi, P. Wang, L. R. Jensen, M. Johansen, C. K. Christensen, Y. Zhang, D. B. Ravnsbæk and Y. Yue, *Adv. Mater.*, 2022, **34**, 2110048.
53 C. Y. Zhou, W. Zong, G. Y. Zhou, X. S. Fan and Y. E. Miao, *Compos. Commun.*, 2021, **25**, 100696.
54 R. Xu, X. Q. Zhang, X. B. Cheng, H. J. Peng, C. Z. Zhao, C. Yan and J. Q. Huang, *Adv. Funct. Mater.*, 2018, **28**, 1705838.
55 Y. Liu, Y. Xu, J. Wang, Y. Sun, X. Feng and H. Xiang, *Mater. Today Sustain.*, 2022, **18**, 100127.
56 H. J. Zhao, G. D. Zhao, F. Q. Liu, F. F. Lan, J. J. Zhou and L. Li, *Chem. Eng. J.*, 2024, **490**, 151559.
57 N. Wei, J. Hu, M. Zhang, J. He and P. Ni, *Electrochim. Acta*, 2019, **307**, 495–502.
58 J. Allen, *Energy Rep.*, 2020, **6**, 217–224.
59 S. C. Zhang, S. Y. Li and Y. Y. Lu, *eScience*, 2021, **1**, 163–177.
60 S. Y. Cheng, R. Deng, Z. Zhang, Q. W. He, Y. F. Zheng, H. Y. Liao, X. T. Fu, J. N. Lu, Y. M. Jiang and Y. H. Gao, *J. Power Sources*, 2024, **614**, 234964.

